DOI: https://doi.org/10.14311/TPFM.2025.002

ON THE CHOICE OF THE HIGHER ORDER DMD MODE PART FOR PROJECTION TO PHYSICAL COORDINATES

M. Belda [1,2], T. Hlavatý [1], M. Isoz [1], T. Hyhlík [2]

[1] **Institute of Thermomechanics, Czech Academy of Sciences, Dolejškova 1402/5, 182 00 Prague 8 – Libeň, Czech Republic**

[2] **Department of Fluid Dynamics and Thermodynamics, Faculty of Mechanical Engineering, Czech Technical University in Prague, Technická 1902/4, 160 00 Prague 6 – Dejvice, Czech Republic**

Abstract

Higher-order dynamic mode decomposition (HODMD) was proposed as a more robust extension of classical dynamic mode decomposition (DMD) designed to overcome DMD's main weaknesses, i.e. susceptibility to noise and inability to capture highly non-linear dynamics. In this study, we try to tie up one of the remaining loose ends of the HODMD. Particularly, each HODMD mode comprises multiple parts that can be projected back to the physical coordinates. Consequently, there is an apparent ambiguity in which part of the HODMD mode to select for projection back to physical coordinates. This ambiguity is present even in the most recent literature and is nowhere explained properly. However, we state a lemma, supported by proof, that the choice of the HODMD mode part does not matter. Then, the equivalence of HODMD mode parts is illustrated on a HODMD analysis of a wake behind a cylinder in a crossflow at Re $\approx$ 5000.

Keywords: Dynamic mode decomposition, Higher-order dynamic mode decomposition, CFD.

1 Introduction

Dynamic mode decomposition (DMD) has been gaining popularity in the fluid dynamics community since the discovery of stable and computationally tractable DMD algorithm in the early 2010s. Its characteristics of a purely data-driven, model-free algorithm that extracts spatio-temporal patterns from the provided data in the form of single-frequency modes make it highly suitable for model order reduction and flow field analysis [1, 2]. Furthermore, most of the important flow information tends to be captured within relatively few DMD modes, especially in cases that exhibit periodic behavior, making DMD suitable for highly efficient data storage from large transient flow simulations [3]. However, there are some inherent drawbacks to DMD. For example, it does poorly in cases with highly non-linear dynamics or noisy input data, which are both rather common in engineering practice.

Higher-order DMD (HODMD) was developed by Le Clainche and Vega [4] as a more robust variant of DMD capable of processing a wider range of problems even in the presence of noisy data and/or complex dynamics [5]. Those characteristics are typical of combustion flows and fluid-structure interactions, where the usability of HODMD was studied, for example, by Corrochano et al. [5] and Rodríguez-López et al. [6]. Then, multiple algorithms for HODMD were quickly developed; see, e.g., [5, 7] or [8].

As in any relatively new method, HODMD lacks proper guidance in some steps of its setup. For example, each snapshot $\boldsymbol{x}_k \in \mathbb{C}^m$, m being the spatial complexity of the system, depends on previous d snapshots, where d is the order of the method and is problem-dependent. Although some general guidance on this is given by Corrochano et al. [5], there is no universally accepted rule yet. Furthermore, each HODMD mode $\boldsymbol{q}_j$ comprises d parts (submodes) that can be projected back to the physical coordinates. The selection of the appropriate part of the higher-order mode for the projection is accompanied by direct contradictions in even the most recent existing literature – see the discrepancy between Corrochano et al. [5] and Jones and Utyuzhnikov [9]. Moreover, even the most recent books, such as [10], do not provide a rigorous explanation.

In this paper, our goal is to address the proper choice of the HODMD mode part for the projection back to the physical coordinates. The hypothesis is stated that, from a mathematical point of view, this choice does not matter. This hypothesis is formulated as a lemma and is subsequently proven. The lemma and its proof are supported by a visual illustration of an example case of turbulent flow behind a cylinder in crossflow.

2 Dynamic mode decomposition and related techniques

Dynamic mode decomposition (DMD) is based on the Koopman assumption. This assumption states that it is possible to project the finite-dimensional nonlinear dynamics onto an infinite-dimensional Hilbert space, where the operator governing the system is linear; effectively trading nonlinearity for infinite-dimensionality [11]. DMD has been proven to find the best-fit finite-dimensional approximation to the eigenmodes of this infinite-dimensional operator. This is a cornerstone of all DMD-based methods. Although the primary focus of this contribution is the higher-order DMD, to provide a wider context for the method, we will start with a description of the classical DMD.

2.1 Data preprocessing

Let us assume a data matrix $\boldsymbol{Y} = [\boldsymbol{x}_1, \boldsymbol{x}_2, \dots, \boldsymbol{x}_n] \in \mathbb{C}^{m\times n}$ and mark each column of $\boldsymbol{Y}$ a snapshot of a dynamical system. In this notation, m is the spatial complexity of the system and n is the number of snapshots. Snapshots are acquired with a constant sampling period Δt. The data matrix $\boldsymbol{Y}$ is denoised using reduced singular value decomposition (SVD) by only retaining ℓ largest singular values,

$$\boldsymbol{Y} = \boldsymbol{\Psi}_\ell \boldsymbol{\Sigma}_\ell \boldsymbol{\Phi}_\ell^H, \quad \boldsymbol{\Psi}_\ell \in \mathbb{C}^{m\times\ell}, \quad \boldsymbol{\Phi}_\ell \in \mathbb{C}^{n\times\ell}, \quad \boldsymbol{\Sigma}_\ell \in \mathbb{R}^{\ell\times\ell}, \quad \ell \le r = \operatorname{rank}(\boldsymbol{Y}). \tag{1}$$

The number of retained singular values ℓ arises from an appropriate condition applied to the diagonal matrix of singular values $\boldsymbol{\Sigma} = \operatorname{diag}(\sigma_1, \dots, \sigma_r) \in \mathbb{R}^{r\times r}$; see, for example, [9] and [12]. For this article, energy criterion based on [9] with cutoff threshold $\varepsilon_{\mathrm{SVD}}$ is used:

$$\frac{\sum_{j=1}^{\ell} \sigma_j^2}{\sum_{j=1}^{r} \sigma_j^2} \ge 1 - \varepsilon_{\mathrm{SVD}}. \tag{2}$$

Matrix of denoised reduced snapshots is then defined as

$$\hat{\boldsymbol{Y}} = \boldsymbol{\Psi}_\ell^H \boldsymbol{Y} = \boldsymbol{\Sigma}_\ell \boldsymbol{\Phi}_\ell^H \in \mathbb{C}^{\ell\times n}, \tag{3}$$

which coincides with projecting $\boldsymbol{Y}$ onto a subspace of its column space spanned by the first ℓ terms of the proper orthogonal decomposition (POD) basis of $\boldsymbol{Y}$ – marked $\boldsymbol{\Psi}_\ell$.

2.2 Classical DMD

In this article, we use DMD as derived in [1] and [11]. It relies on the classical Koopman assumption and can also be viewed from the perspective of discrete linear dynamical systems. The DMD aims to find the spectral properties of the best-fit discrete linear operator $\boldsymbol{A}$. For $n+1$ system snapshots $\boldsymbol{x}_i \in \mathbb{C}^m$, $i = 0, 1, \dots, n$, the operator $\boldsymbol{A}$ is defined as

$$\begin{gathered}\boldsymbol{A} : \mathbb{C}^m \to \mathbb{C}^m; \quad \boldsymbol{A} \coloneqq \underset{\mathcal{A}\in\mathbb{C}^{m\times m}}{\arg\min} \sum_{j=0}^{n-1} \|\mathcal{A}\boldsymbol{x}_j - \boldsymbol{x}_{j+1}\|_2^2 = \underset{\mathcal{A}\in\mathbb{C}^{m\times m}}{\arg\min} \|\mathcal{A}\boldsymbol{X} - \boldsymbol{Y}\|_F^2 \\ \text{where} \\ \boldsymbol{X} = [\boldsymbol{x}_0, \boldsymbol{x}_1, \dots, \boldsymbol{x}_{n-1}] \in \mathbb{C}^{m\times n},\ \boldsymbol{Y} = [\boldsymbol{x}_1, \boldsymbol{x}_2, \dots, \boldsymbol{x}_n] \in \mathbb{C}^{m\times n},\ \|\bullet\|_F \dots \text{Frobenius norm}\end{gathered} \tag{4}$$

Now, let $\boldsymbol{A}$ be diagonalizable, i.e., $\boldsymbol{A} = \boldsymbol{V}\boldsymbol{\Lambda}\boldsymbol{V}^{-1}$, where columns of $\boldsymbol{V}$ contain eigenvectors of $\boldsymbol{A}$, $\boldsymbol{\Lambda}$ is the diagonal matrix of eigenvalues and $r = \operatorname{rank}(\boldsymbol{A})$. Then the following holds [1],

$$\begin{gathered}\boldsymbol{x}_k = \boldsymbol{A}^k \boldsymbol{x}_0 = \boldsymbol{V}\boldsymbol{\Lambda}^k\boldsymbol{V}^{-1}\boldsymbol{x}_0 = \boldsymbol{V}\boldsymbol{\Lambda}^k\boldsymbol{b} = \sum_{j=1}^{r} \lambda_j^k b_j \boldsymbol{v}_j, \\ \text{with the triplets}\,(\lambda_j; \boldsymbol{v}_j; b_j) \in \mathbb{C} \times \mathbb{C}^m \times \mathbb{C}.\end{gathered} \tag{5}$$

If $\ell < r$ instead of r terms are used in the sum on the right-hand side of (5), then this sum yields a low-rank representation of the original data by using data triplets, i.e. eigenvalue, eigenvector, and eigenvector amplitude.

The direct computation of $\boldsymbol{A}$ and its eigendecomposition is costly, which is why the DMD is employed. The DMD computes matrix $\hat{\boldsymbol{A}}$, which is the low-rank approximation of $\boldsymbol{A}$. This is done using the reduced SVD introduced in (1) on matrix $\boldsymbol{X}$,

$$\begin{gathered}\boldsymbol{X} = \boldsymbol{\Psi}_\ell \boldsymbol{\Sigma}_\ell \boldsymbol{\Phi}_\ell^H , \quad \boldsymbol{\Psi}_\ell \in \mathbb{C}^{m\times\ell}, \quad \boldsymbol{\Phi}_\ell \in \mathbb{C}^{n\times\ell}, \quad \boldsymbol{\Sigma}_\ell \in \mathbb{R}^{\ell\times\ell}, \quad \ell \le r = \operatorname{rank}(\boldsymbol{X}), \\ \text{and subsequently } \hat{\boldsymbol{A}} = \boldsymbol{\Psi}_\ell^H \boldsymbol{A} \boldsymbol{\Psi}_\ell = \boldsymbol{\Psi}_\ell^H \boldsymbol{Y} \boldsymbol{\Phi}_\ell \boldsymbol{\Sigma}_\ell^{-1} \in \mathbb{C}^{\ell\times\ell} .\end{gathered} \tag{6}$$

Note that it can be proven that when $\ell = r$, the nonzero eigenvalues of $\hat{\boldsymbol{A}}$ coincide with the nonzero eigenvalues of $\boldsymbol{A}$, thus $\hat{\boldsymbol{A}}$ contains all information about the system dynamics [1]. The DMD data triplets, i.e. eigenvalue, eigenmode, and mode amplitude, which are an approximation of the eigendecomposition triplets in (5), are

$$(\lambda_j; \boldsymbol{\vartheta}_j; a_j) \in \mathbb{C} \times \mathbb{C}^m \times \mathbb{C} . \tag{7}$$

2.3 Higher-order DMD

Higher-order DMD (HODMD) as derived by Le Clainche and Vega [4] is a natural extension of classical DMD. Classical DMD seeks a best-fit one-step-in-time-advancing operator. In HODMD, the current snapshot is assumed to depend on more than one previous snapshot. In other words, the higher-order Koopman assumption for the original data states that $\boldsymbol{x}_{k+d} = \sum_{j=1}^{d} \boldsymbol{A}_j \boldsymbol{x}_{k+j-1}$ where $\boldsymbol{A}_j$ behave similarly to the DMD matrix $\boldsymbol{A}$, i.e. evaluate the contribution of snapshot $\boldsymbol{x}_{k+j-1}$ to snapshot $\boldsymbol{x}_{k+d}$ [4]. Note, that when $d = 1$, the HODMD reduces back to the classical DMD. The higher-order Koopman assumption can be premultiplied by the POD basis $\boldsymbol{\Psi}_\ell^H$ from (3) to yield

$$\hat{\boldsymbol{x}}_{k+d} = \boldsymbol{\Psi}_\ell^H \boldsymbol{x}_{k+d} = \sum_{j=1}^{d} \boldsymbol{\Psi}_\ell^H \boldsymbol{A}_j \boldsymbol{\Psi}_\ell \boldsymbol{\Psi}_\ell^H \boldsymbol{x}_{k+j-1} = \sum_{j=1}^{d} \hat{\boldsymbol{A}}_j \hat{\boldsymbol{x}}_{k+j-1} \in \mathbb{C}^\ell . \tag{8}$$

Now, the higher-order time-advancing operator can be defined as $\tilde{\boldsymbol{x}}_{k+1} = \tilde{\boldsymbol{A}} \tilde{\boldsymbol{x}}_k$, where the block structure of $\tilde{\boldsymbol{A}} \in \mathbb{C}^{\ell d\times\ell d}$ and $\tilde{\boldsymbol{x}}_k \in \mathbb{C}^{\ell d}$ are

$$\tilde{\boldsymbol{A}} = \begin{bmatrix} 0 & \boldsymbol{I} & 0 & \cdots & 0 \\ 0 & 0 & \boldsymbol{I} & \cdots & 0 \\ 0 & 0 & 0 & \ddots & \vdots \\ \vdots & \vdots & \vdots & \ddots & \boldsymbol{I} \\ \hat{\boldsymbol{A}}_1 & \hat{\boldsymbol{A}}_2 & \hat{\boldsymbol{A}}_3 & \cdots & \hat{\boldsymbol{A}}_d \end{bmatrix}, \quad \tilde{\boldsymbol{x}}_k = \begin{bmatrix} \hat{\boldsymbol{x}}_k \\ \hat{\boldsymbol{x}}_{k+1} \\ \vdots \\ \hat{\boldsymbol{x}}_{k+d-1} \end{bmatrix}, \quad \boldsymbol{q}_j = \begin{bmatrix} \hat{\boldsymbol{q}}_j^1 \\ \hat{\boldsymbol{q}}_j^2 \\ \vdots \\ \hat{\boldsymbol{q}}_j^d \end{bmatrix} \tag{9}$$

The eigenvalues of $\tilde{\boldsymbol{A}}$ define the spectral properties of the system, and the eigenvectors, marked $\boldsymbol{q}_j$, define the HODMD modes. As with DMD, direct evaluation of $\tilde{\boldsymbol{A}}$ and its eigendecomposition is costly. The computing costs are mitigated using an approach similar to the classical DMD, i.e., a second denoising and dimensionality reduction, see (6). After this step, we obtain HODMD modes $\boldsymbol{q}_j \in \mathbb{C}^{\ell d}$, $j = 1, 2, \ldots, p$ where each of them comprises d submodes $\hat{\boldsymbol{q}}_j^1, \ldots, \hat{\boldsymbol{q}}_j^d$; see (9).

Finally, to reconstruct the data in the physical space, HODMD modes and eigenvalues need to be supplemented by HODMD amplitudes, see (5). HODMD amplitudes are computed by least-squares fitting over the system snapshots. In particular, the equivalent of (5) for HODMD is

$$\hat{\boldsymbol{x}}_k = \sum_{j=1}^{p} \lambda_j^{k-1} a_j \hat{\boldsymbol{q}}_j , \quad k = 1, 2, \ldots, n - d + 1 , \tag{10}$$

where a_j is amplitude of mode j and $\hat{\boldsymbol{q}}_j \in \mathbb{C}^\ell$ is one of the submodes $\hat{\boldsymbol{q}}_j^1, \ldots, \hat{\boldsymbol{q}}_j^d$ of the HODMD mode $\boldsymbol{q}_j$ with a dimension suitable for projection into physical coordinates selected by a yet-undefined manner.

From (10), the relationship $\boldsymbol{L}\boldsymbol{a} = \hat{\boldsymbol{y}}$ can be defined, which is an overdetermined problem to be solved in a least-squares sense by applying pseudoinverse of $\boldsymbol{L}$,

$$\boldsymbol{L} = \begin{bmatrix} \boldsymbol{Q} \\ \boldsymbol{Q}\boldsymbol{\Lambda} \\ \vdots \\ \boldsymbol{Q}\boldsymbol{\Lambda}^{s-1} \end{bmatrix}, \quad \boldsymbol{a} = \begin{bmatrix} a_1 \\ \vdots \\ a_p \end{bmatrix}, \quad \hat{\boldsymbol{y}} = \begin{bmatrix} \hat{\boldsymbol{x}}_1 \\ \vdots \\ \hat{\boldsymbol{x}}_s \end{bmatrix}, \quad \boldsymbol{Q} = [\hat{\boldsymbol{q}}_1, \ldots, \hat{\boldsymbol{q}}_p], \quad \boldsymbol{\Lambda} = \operatorname{diag}(\lambda_1, \ldots, \lambda_p) , \tag{11}$$

where $s \leq n$ is the number of snapshots used for amplitude-fitting.

2.4 Physical meaning of eigenvalues λ

The eigenvalues of system matrix $\boldsymbol{A}$ ($\tilde{\boldsymbol{A}}$ for HODMD) carry all information about the time evolution of the associated mode, i.e. growth or decay rate and frequency. This can be inferred from the theory of discrete linear systems. Stable modes have $|\lambda| \leq 1$ indicating decaying or constant amplitude, unstable modes have $|\lambda| > 1$ and are highly undesirable in real physical systems. The frequency of the mode is given by the angle of the complex number λ and the sampling period Δt,

$$f = \frac{\arg(\lambda)}{2\pi\Delta t}\,. \tag{12}$$

3 Ambiguity in projection to physical coordinates

The ambiguity arises when the HODMD modes $\boldsymbol{q}_k \in \mathbb{C}^{\ell d}$ defined in (9) are projected to physical coordinates. This projection is done in the same way as the projection of the reduced snapshots to physical coordinates, i.e. $\boldsymbol{\vartheta}_k = \boldsymbol{\Psi}_\ell \hat{\boldsymbol{q}}_k$. However, the projection matrix $\boldsymbol{\Psi}_\ell$ only accepts vectors/matrices with ℓ rows as operands. Since the whole HODMD mode $\boldsymbol{q}_k$ has a dimension of ℓd, it is necessary to choose only one of the submodes $\hat{\boldsymbol{q}}_k^1, \ldots, \hat{\boldsymbol{q}}_k^d \in \mathbb{C}^\ell$ – designated as $\hat{\boldsymbol{q}}_k$. For this choice, there is no universally accepted rule.

Lemma: Let us consider the eigenvalue problem for $\tilde{\boldsymbol{A}}$ in the form of $\tilde{\boldsymbol{A}}\boldsymbol{q} = \lambda \boldsymbol{q}$, $\lambda \neq 0$. Then, all submodes $\hat{\boldsymbol{q}}_k^1, \ldots, \hat{\boldsymbol{q}}_k^d$ constituting the mode $\boldsymbol{q}_k$ can be projected on each other as $\hat{\boldsymbol{q}}_k^i = \lambda_k^{i-j}\hat{\boldsymbol{q}}_k^j$, where $i, j = 1, 2, \ldots, d$ and the subscript k designates the k-th eigenvalue-eigenmode pair.

Proof: When the eigenvalue problem is rewritten using the relations (9) we obtain

$$\begin{bmatrix} 0 & \boldsymbol{I} & 0 & \cdots & 0 \\ 0 & 0 & \boldsymbol{I} & \cdots & 0 \\ 0 & 0 & 0 & \ddots & \vdots \\ \vdots & \vdots & \vdots & \ddots & \boldsymbol{I} \\ \hat{\boldsymbol{A}}_1 & \hat{\boldsymbol{A}}_2 & \hat{\boldsymbol{A}}_3 & \cdots & \hat{\boldsymbol{A}}_d \end{bmatrix} \begin{bmatrix} \hat{\boldsymbol{q}}_k^1 \\ \hat{\boldsymbol{q}}_k^2 \\ \vdots \\ \hat{\boldsymbol{q}}_k^{d-1} \\ \hat{\boldsymbol{q}}_k^d \end{bmatrix} = \begin{bmatrix} \hat{\boldsymbol{q}}_k^2 \\ \hat{\boldsymbol{q}}_k^3 \\ \vdots \\ \hat{\boldsymbol{q}}_k^d \\ \hat{\boldsymbol{A}}_1\hat{\boldsymbol{q}}_k^1 + \cdots + \hat{\boldsymbol{A}}_d\hat{\boldsymbol{q}}_k^d \end{bmatrix} = \lambda_k \begin{bmatrix} \hat{\boldsymbol{q}}_k^1 \\ \hat{\boldsymbol{q}}_k^2 \\ \vdots \\ \hat{\boldsymbol{q}}_k^{d-1} \\ \hat{\boldsymbol{q}}_k^d \end{bmatrix}, \tag{13}$$

which yields

$$\hat{\boldsymbol{q}}_k^2 = \lambda_k \hat{\boldsymbol{q}}_k^1,\ \hat{\boldsymbol{q}}_k^3 = \lambda_k \hat{\boldsymbol{q}}_k^2, \ldots,\ \hat{\boldsymbol{q}}_k^d = \lambda_k \hat{\boldsymbol{q}}_k^{d-1}, \quad \text{i.e.,} \quad \hat{\boldsymbol{q}}_k^i = \lambda_k^{i-1}\hat{\boldsymbol{q}}_k^1,\ i = 1, 2, \ldots, d\,. \tag{14}$$

Now, noting that $\hat{\boldsymbol{q}}_k^1$ can be expressed from (14) as

$$\hat{\boldsymbol{q}}_k^1 = \frac{\hat{\boldsymbol{q}}_k^j}{\lambda_k^{j-1}}, \qquad j = 1, 2, \ldots, d\,, \tag{15}$$

equations (14) and (15) can be combined into

$$\hat{\boldsymbol{q}}_k^i = \lambda_k^{i-1}\hat{\boldsymbol{q}}_k^1 = \frac{\lambda_k^{i-1}}{\lambda_k^{j-1}}\hat{\boldsymbol{q}}_k^j = \lambda_k^{i-j}\hat{\boldsymbol{q}}_k^j, \qquad i, j = 1, 2, \ldots, d\,, \tag{16}$$

which proves the lemma. □

Based on this proof, it can be stated that for the purpose of projection back to the physical coordinates, all parts of the HODMD mode $\boldsymbol{q}_k$ are equivalent. Furthermore, from equation (5), it can be inferred that each multiplication by eigenvalue means shifting one step in time. Thus, all submodes $\hat{\boldsymbol{q}}_k^1, \ldots, \hat{\boldsymbol{q}}_k^d$ are in fact one vector, only shifted to different positions in time.

4 Comparison of different submodes of first HODMD mode

In this section, we provide a visual illustration of the Lemma stated in section 3. In particular, we build on the results of Hlavatý et al. [13] and study the turbulent wake behind a circular cylinder in a cross flow at Re = 4815. We focus on the first HODMD mode and compare its different parts against each other and against the first POD mode.

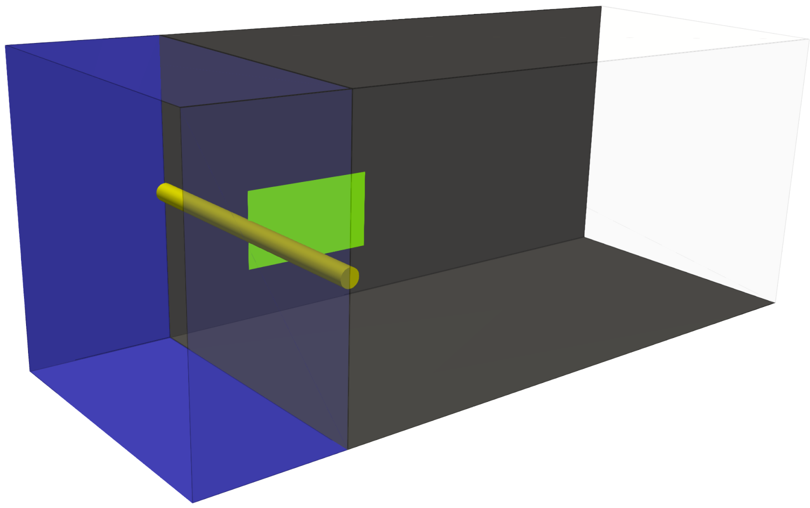

Figure 1: Sketch of the computational domain. Slip parts of the walls are in blue. The plane of interest is green. Image inspired by Hlavatý et al. [13].

4.1 Computation setup

The complete modal analysis performed stems from a flow simulated in a digital twin of an experimental test section of $25 \times 25 \times 300$ cm. In this test section, a 15 mm diameter cylinder is placed that spans the entirety of it. The turbulent flow is simulated by a numerical solution of the isothermal and incompressible Navier-Stokes equations for a Newtonian fluid. Turbulence was modeled by detached eddy simulation (DES) in the formulation of [14]. The solution itself is based on the finite volume method.

The geometry of the problem, including the plane of interest on which we sampled the data for subsequent analyses, is shown in Figure 1. Note the presence of blue "slip walls" that were added to the computational domain to account for the nozzle used in the experiment to generate uniform flow at the contact with the cylinder.

The computational mesh was prepared in a way to simulate most of the plane of interest with the resolution of the direct numerical simulation of the flow. The remainder of the examined region was well within the domain of large eddy simulation. The DES approach itself was applied merely to supply the examined region, that is, the plane of interest, with physically suitable boundary conditions, while allowing one to directly set well-defined boundary conditions at the test section boundaries. For the exact computational setup used, and for the verification and validation of the flow model itself, the reader is referred to [13].

4.2 HODMD decomposition of computed flow field

Data preprocessing Since the original experimental data in [13] was obtained using time-resolved particle image velocimetry, only the x (streamwise) and y (transverse) components of the velocity field were analyzed. Then, in agreement with [15] and [13], the data were symmetrized with respect to the assumed horizontal symmetry plane prior to modal decomposition. Finally, the energy content criterion for SVD truncation (2) has been used to denoise the input data. The threshold value of $\varepsilon_{\mathrm{SVD}} = 10^{-3}$ was applied, which means that 99.9 % of the original flow field energy is retained.

HODMD parameters The setup and use of HODMD is more complicated than that of POD, as there are several free parameters that POD does not have. In addition to the $\varepsilon_{\mathrm{SVD}}$ threshold in data denoising, the order of HODMD was set as $d = 120$ and the number of snapshots for amplitude-fitting was set as $s = 560$. Unlike classical DMD, where the spatial complexity of data has to be strictly greater than the spectral complexity, HODMD does not have such a limitation, as long as both spatial and spectral complexities are finite [4]. Data processing has been carried out on 4000 snapshots sampled at $f_{\mathrm{s}} = 2$kHz, representing a total of 2 s of fluid flow.

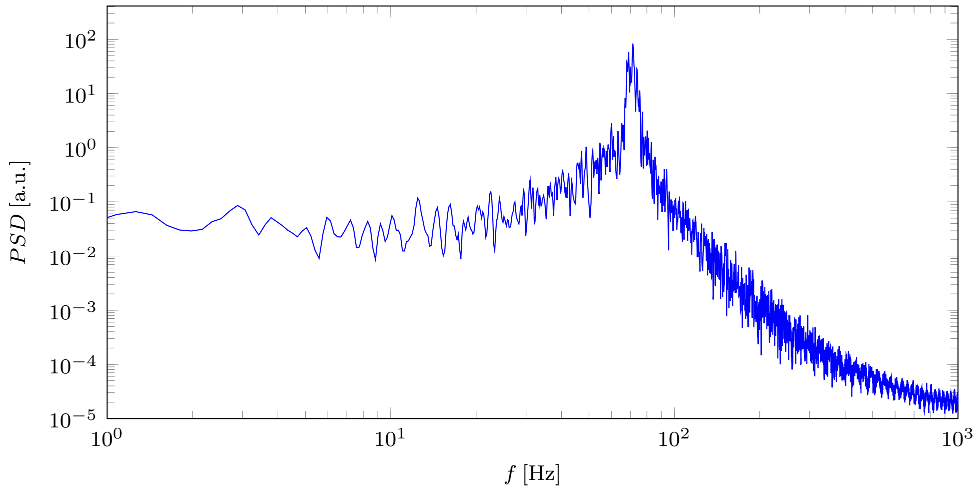

Figure 2: Power spectral density of POD mode 1

Supplementary POD analysis To provide a reference point for the presented HODMD results, we also show the first POD mode. The spectrum of the temporal part of the mode is shown in Figure 2. The main peak of the POD spectrum is at $f_{\mathrm{POD}} = 71.4\,\mathrm{Hz}$ while the theoretical vortex shedding frequency is $f_{\mathrm{St}} = 69.4\,\mathrm{Hz}$ [13].

HODMD analysis Submodes $\hat{\boldsymbol{q}}_1^1$, $\hat{\boldsymbol{q}}_1^{15}$ and $\hat{\boldsymbol{q}}_1^{29}$ of the first antisymmetric HODMD mode are compared after projection to physical coordinates; see Figure 3 – modes in physical coordinates are designated $\boldsymbol{\vartheta}_1^1$, $\boldsymbol{\vartheta}_1^{15}$ and $\boldsymbol{\vartheta}_1^{29}$ in accordance with (7). The frequency of the first mode is $f_1 = 71.35\,\mathrm{Hz}$, which is close to both the peak in the POD frequency spectrum and the theoretical vortex shedding frequency. Furthermore, the sampling rate is 28.031 samples per period of the first mode, which is very close to being a whole number. Thus, the subvector $\boldsymbol{\vartheta}_1^{29}$ should be almost the same as $\boldsymbol{\vartheta}_1^1$ since it is shifted from $\boldsymbol{\vartheta}_1^1$ by 28 time steps, and $|\lambda_1| = 1$, which is to be expected of a periodic flow field. The similarity of $\boldsymbol{\vartheta}_1^1$ and $\boldsymbol{\vartheta}_1^{29}$ is apparent from the comparison of Figures 3a and c and is further documented by the calculated difference $\left\|\boldsymbol{\vartheta}_1^1 - \boldsymbol{\vartheta}_1^{29}\right\|_2 = 0.0075$ where $\boldsymbol{\vartheta}_1^1$ is a unit vector.

Vectors $\boldsymbol{\vartheta}_1^1$ and $\boldsymbol{\vartheta}_1^{15}$ should be exactly out-of-phase – having opposite signs to each other; see Figures 3a and b. When the shape of $\boldsymbol{\vartheta}_1^1$ and $\boldsymbol{\vartheta}_1^{15}$ is compared, the $\left\|\boldsymbol{\vartheta}_1^1 + \boldsymbol{\vartheta}_1^{15}\right\|_2 = 0.0038$ where the + sign accounts for the sign flip caused by the half-period shift.

This difference ($\lesssim 1.0\%$ between $\boldsymbol{\vartheta}_1^1$ and $\boldsymbol{\vartheta}_1^{29}$; $\lesssim 0.5\%$ between $\boldsymbol{\vartheta}_1^1$ and $\boldsymbol{\vartheta}_1^{15}$) can be explained by the fact that the phase shift between these vectors is very close to being a multiple of half-period, but not exactly so. This means that $\boldsymbol{\vartheta}_1^1$ and $\boldsymbol{\vartheta}_1^{29}$ are not exactly one period apart, introducing a small phase shift between them. This explanation is further supported by the fact that the difference between $\boldsymbol{\vartheta}_1^1$ and $\boldsymbol{\vartheta}_1^{15}$, where the phase shift error is half that mentioned above, is almost exactly half the difference between $\boldsymbol{\vartheta}_1^1$ and $\boldsymbol{\vartheta}_1^{29}$ – see the calculated differences and Figure 4.

Finally, the distinctiveness of the peak in the first POD mode visible in Figure 2 hints at the similarity of the spatial part of the POD mode to $\boldsymbol{\vartheta}_1^1$ and $\boldsymbol{\vartheta}_1^{29}$ or $\boldsymbol{\vartheta}_1^{15}$, cf. Figure 3a-c to d.

5 Conclusions

In this contribution, we have discussed the ambiguity in selecting the appropriate part of the HODMD mode for projection back to the physical coordinates. In particular, a lemma was proposed that all submodes of the HODMD mode can be recursively projected onto each other via eigenvalue λ. The lemma was proven using the structure of the HODMD system matrix and modes, thus clarifying the issue of ambiguity in the choice of the HODMD submode. The lemma and its proof were supplemented by a visual comparison of different parts of the first antisymmetric HODMD mode of the turbulent wake behind a circular cylinder in a crossflow at Re $\approx$ 5000. As expected, all the compared submodes are equivalent. Furthermore, they are similar to the first antisymmetric mode obtained by the proper orthogonal decomposition of the same dataset.

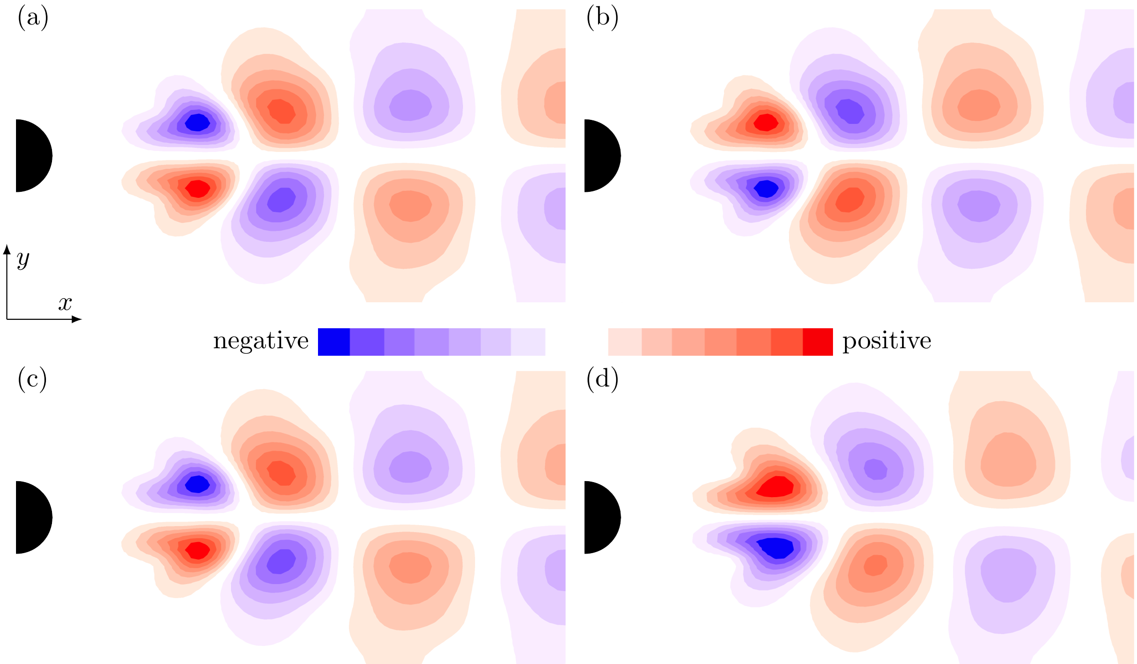

Figure 3: Comparison of x components of (a) $\boldsymbol{\vartheta}_1^1$, (b) $\boldsymbol{\vartheta}_1^{15}$ and (c) $\boldsymbol{\vartheta}_1^{29}$ parts of HODMD mode 1 with (d) x component of POD mode 1.

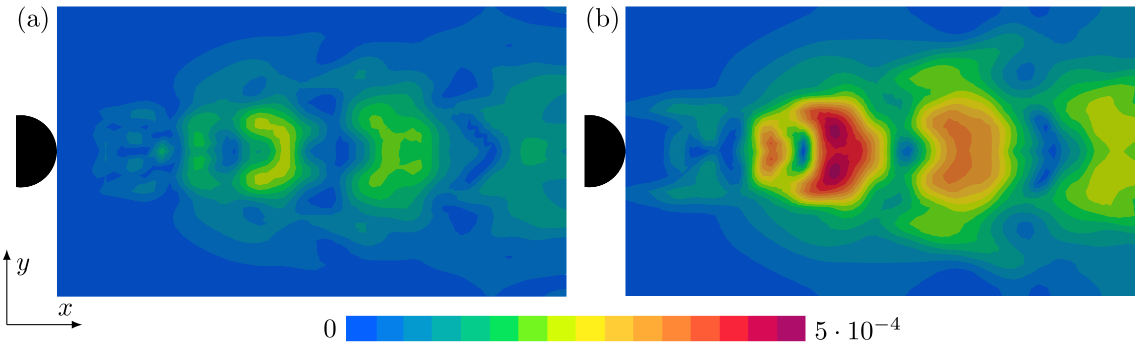

Figure 4: Difference between (a) $\boldsymbol{\vartheta}_1^1$ and $\boldsymbol{\vartheta}_1^{15}$ and (b) $\boldsymbol{\vartheta}_1^1$ and $\boldsymbol{\vartheta}_1^{29}$ – magnitude distribution

Acknowledgment

The authors acknowledge the financial support provided by the Ministry of Education, Youth, and Sports of the Czech Republic via the project No. CZ.02.01.01/00/23_020/0008501 (METEX), co-funded by the European Union. The work was financially supported by the institutional support RVO:61388998, by the Czech Science Foundation (GA 25-17815S), and by the grant project with No. TN02000069/001N of the Technology Agency of the Czech Republic. This work was supported by the Grant Agency of the Czech Technical University in Prague, grant No. SGS OHK2-021/25.

References

[1] Krake, T., Weiskopf, D. & Eberhardt, B.: Dynamic mode decomposition: Theory and data reconstruction. *Arxiv.* (2022). doi: 10.48550/arXiv.1909.10466.

[2] Wu, Z., Lawrence, D., Utyuzhnikov, S. & Afgan, I.: Proper orthogonal decomposition and dynamic mode decomposition of jet in channel crossflow. *Nuclear Engineering and Design.* vol. 344 no. 1: (2019). pp. 54–68. doi: 10.1016/j.nucengdes.2019.01.015.

[3] Li, C. Y., Tse, T. K. & Hu, G.: Dynamic mode decomposition on pressure flow field analysis: Flow field reconstruction, accuracy, and practical significance. *Journal of Wind Engineering and Industrial Aerodynamics.* vol. 205: (2020). page 104278. doi: 10.1016/j.jweia.2020.104278.

[4] Le Clainche, S. & Vega, J. M.: Higher order dynamic mode decomposition. *SIAM Journal on Applied Dynamical Systems.* vol. 16 no. 2: (2017). pp. 882–925. doi: 10.1137/15M1054924.

[5] Corrochano, A., D'Alessio, G., Parente, A. & Clainche, S. L.: Higher order dynamic mode decomposition to model reacting flows. *International Journal of Mechanical Sciences.* vol. 249: (2023). page 108219. doi: 10.1016/j.ijmecsci.2023.108219.

[6] Rodríguez-López, E., Carter, D. W. & Ganapathisubramani, B.: Dynamic mode decomposition-based reconstructions for fluid–structure interactions: An application to membrane wings. *Journal of Fluids and Structures.* vol. 104: (2021). page 103315. doi: 10.1016/j.jfluidstructs.2021.103315.

[7] Li, K. & Utyuzhnikov, S.: Tensor train-based higher-order dynamic mode decomposition for dynamical systems. *Mathematics.* (2023). doi: 10.3390/math11081809.

[8] Amor, C., Schlatter, P., Vinuesa, R. & Clainche, S. L.: Higher-order dynamic mode decomposition on-the-fly: A low-order algorithm for complex fluid flows. *Journal of Computational Physics.* vol. 475: (2023). page 111849. doi: 10.1016/j.jcp.2022.111849.

[9] Jones, C. & Utyuzhnikov, S.: Application of higher order dynamic mode decomposition to modal analysis and prediction of power systems with renewable sources of energy. *International Journal of Electrical Power & Energy Systems.* vol. 138: (2022). page 107925. doi: 10.1016/j.ijepes.2021.107925.

[10] Vega, J. M. & Clainche, S. L. *Higher Order Dynamic Mode Decomposition and Its Applications.* Academic Press: London, UK: (2020). ISBN 978-0-12-819743-1.

[11] Benner, P., Grivet-Talocia, S., Quarteroni, A., Rozza, G. & Schilders, W. *Model Order Reduction*: volume 2. de Gruyter: Berlin, Germany: (2021). ISBN 978-3-11-067140-7.

[12] Le Clainche, S., Vega, J. M. & Soria, J.: Higher order dynamic mode decomposition of noisy experimental data: The flow structure of a zero-net-mass-flux jet. *Experimental Thermal and Fluid Science.* vol. 88: (2017). pp. 336 – 353. doi: 10.1016/j.expthermflusci.2017.06.011.

[13] Hlavatý, T., Isoz, M., Belda, M., Uruba, V. & Procházka, P.: Is the proper orthogonal decomposition suitable to validate simulation of turbulent wake? *Journal of Wind Engineering and Industrial Aerodynamics.* vol. 255: (2024). page 105953. doi: 10.1016/j.jweia.2024.105953.

[14] Strelets, M. *Detached eddy simulation of massively separated flows*: pp. 2001–0879. AIAA: (2001).

[15] Bourgeois, J. A., Noack, B. R. & Martinuzzi, R. J.: Generalized phase average with applications to sensor-based flow estimation of the wall-mounted square cylinder wake. *Journal of Fluid Mechanics.* vol. 736: (2013). page 316–350. doi: 10.1017/jfm.2013.494.